EPJ manuscript No.
(will be inserted by the editor)

α-cluster states in ^{46,54}Cr from double-folding potentials

Peter Mohr[1,2a]

[1] Diakonie-Klinikum, D-74523 Schwäbisch Hall, Germany
[2] Institute for Nuclear Research (Atomki), H-4001 Debrecen, Hungary

Received: date / Revised version: date

Abstract. α–cluster states in ^{46}Cr and ^{54}Cr are investigated in the double-folding model. This study complements a recent similar work of Souza and Miyake [1] which was based on a specially shaped potential. Excitation energies, reduced widths, intercluster separations, and intra-band transition strengths are calculated and compared to experimental values for the ground state bands in ^{46}Cr and ^{54}Cr. The α-cluster potential is also applied to elastic scattering at low and intermediate energies. Here, as a byproduct, a larger radial extent of the neutron density in ^{50}Ti is found.

PACS. 21.60.Gx Cluster models – 27.40.+z $39 \leq A \leq 58$

1 Introduction

α-clustering is a very well-known phenomenon in nuclear physics which is found in many nuclei across the chart of nuclides [2]. A lot of work has been done for doubly-magic cores, i.e. ^{212}Po = ^{208}Pb $\otimes$ α, ^{44}Ti = ^{40}Ca $\otimes$ α, ^{20}Ne = ^{16}O $\otimes$ α, and ^{8}Be = ^{4}He $\otimes$ α. The wide gap between ^{212}Po and ^{44}Ti was often filled by studies of nuclei with semi-magic ($N = 50$) cores like ^{96}Ru = ^{92}Mo $\otimes$ α or ^{94}Mo = ^{90}Zr $\otimes$ α. A detailed introduction into the nuclear cluster model is provided in a dedicated special issue of Prog. Theor. Phys. Suppl. **132**, [3,4,5,6,7,8,9,10]. Very recently, Souza and Miyake [1] (hereafter: S&M) have extended these studies towards the chromium isotopes. From the Q_A/A_T systematics they have identified ^{46,54}Cr = ^{42,50}Ti $\otimes$ α as preferred nuclei for α-clustering. Their subsequent study finds that ^{46}Cr has a significant degree of α-clustering, whereas the reduced α widths in ^{54}Cr are about a factor of three lower. Interestingly, earlier studies above ^{44}Ti have focused on ^{48}Cr which is considered as a ^{40}Ca core plus two α particles [11,12].

The present study is motivated as an extension of the work of S&M. In the approach by S&M it is first intended to find a two-body potential which is able to reproduce the energies of α-cluster states in ^{46}Cr and ^{54}Cr. This potential is then used to calculate the (quasi-)bound state wave functions $u(r)$ and to derive reduced widths γ_α^2 and θ_α^2 and transition strengths $B(E2)$.

The approach of the present study, i.e., the α-cluster model in combination with double-folding potentials, has been widely used for the above mentioned doubly-magic cores. Properties of ^{8}Be = ^{4}He $\otimes$ α and the ^{4}He(α,γ)^{8}Be capture cross section were calculated in [13]. A detailed study of ^{19}F = ^{15}N $\otimes$ α and ^{20}Ne = ^{16}O $\otimes$ α is given in [14] which was later extended to (α,γ) capture reactions [15,16,17]. ^{44}Ti = ^{40}Ca $\otimes$ α and ^{40}Ca(α,α)^{40}Ca elastic scattering was studied in [18], and the mass region around $A \approx 40$ was also reviewed in detail in [6]. ^{212}Po = ^{208}Pb $\otimes$ α, the α- and γ-decay properties of ^{212}Po, and α-elastic scattering are investigated in [19,20], and a study for ^{104}Te = ^{100}Sn $\otimes$ α is given in [21]. A series of $N = 50 \otimes \alpha$ nuclei were investigated in [20,22,23]. Finally, α-decay properties of nuclei, including superheavy nuclei up to $A \approx 300$, are often described within the folding potential approach (e.g., [24,25,26]).

Here I focus on ^{46}Cr and ^{54}Cr and compare the results of S&M to the results from systematic double-folding potentials. Contrary to the approach of S&M who are able to describe the excitation energies of all states in the ground state band using a specially shaped potential, the double-folding potentials of the present study require a minor L-dependent adjustment to each state under study. This disadvantage of the folding potential is compensated by two advantages: (*i*) The folding potentials can describe not only bound state properties, but also elastic scattering over a wide energy range. (*ii*) The typically smooth variation of the parameters of the folding potentials can be used to identify peculiar properties of the nuclei under study. Consequently, the approaches of S&M and this work should be considered as complementary.

2 Folding potential model

In the present study the interaction between the α particle and the core is calculated from the folding procedure with the widely used energy- and density-dependent DDM3Y

[a] *Email: WidmaierMohr@t-online.de; mohr@atomki.mta.hu*

interaction $v_{\rm eff}$:

$$V_F(r) = \int\int \rho_P(r_P)\,\rho_T(r_T)\,v_{\rm eff}(s,\rho,E_{\rm NN})\;d^3r_P\;d^3r_T \qquad (1)$$

For details of the folding approach, see e.g. [27,28,29].

The densities ρ_P and ρ_T of projectile and target are usually derived from the experimental charge density distributions which are measured by electron scattering and summarized in [30]. However, in the present study, the density of ^{42}Ti for the ^{42}Ti-α potential is not available because ^{42}Ti is unstable and experimentally not yet accessible for electron scattering (although electron scattering for unstable nuclei may become feasible in the near future at the SCRIT facility [31]). In addition, the charge density distribution of ^{50}Ti for the ^{50}Ti-α potential may deviate from the matter density because the N/Z ratio deviates significantly from unity. Therefore, the present work uses theoretical densities as provided as a part of the widely used statistical model code TALYS [32].

The following tests have been made to verify the theoretical density distributions of TALYS. First, the calculations of α-cluster states in ^{44}Ti of our previous work [18] were repeated using the theoretical density of ^{40}Ca from TALYS instead of an experimental density, and only tiny deviations to the results in Tables II and III of [18] were found. Second, folding potentials were calculated for ^{50}Ti-α using either the theoretical density from TALYS or a matter density derived from the experimental charge density [30]. Both potentials were applied to ^{50}Ti(α,α)^{50}Ti elastic scattering at 25 MeV [33], and it was found that a better description of the experimental data was obtained using the theoretical ^{50}Ti density distribution. Further details on elastic scattering will be discussed later in Sect. 4, including scattering data at low and intermediate energies [34,35]. Consequently, after these successful tests, the theoretical density distributions from TALYS were used in the present study.

The total interaction potential $V(r)$ is given by

$$V(r) = V_N(r) + V_C(r) = \lambda\,V_F(r) + V_C(r) \qquad (2)$$

where the nuclear potential V_N is the double-folding potential V_F of Eq. (1) multiplied by a strength parameter $\lambda \approx 1.1 - 1.3$ [18,29]. V_C is the Coulomb potential in the usual form of a homogeneously charged sphere with the Coulomb radius R_C chosen the same as the rms radius of the folding potential V_F.

The strength parameter λ is adjusted to reproduce the energies of the bound states with $E < 0$ and quasi-bound states with $E > 0$ where $E = 0$ corresponds to the threshold of α emission in the compound nucleus. The number of nodes N of the bound state wave function was taken from the Wildermuth condition

$$Q = 2N + L = \sum_{i=1}^{4}(2n_i + l_i) = \sum_{i=1}^{4} q_i \qquad (3)$$

where Q is the number of oscillator quanta, N is the number of nodes, and L is the relative angular momentum of the α-core wave function. $q_i = 2n_i + l_i$ are the corresponding quantum numbers of the nucleons in the α cluster. For the ground state bands of the nuclei in the lower fp-shell I use $q_i = 3$, resulting in $Q = 12$, which leads to seven states with J^π from 0^+ to 12^+ for the even-even nuclei under study. This choice is similar to S&M.

Typically, a smooth decrease of the potential strength parameter λ is found with increasing excitation energy or increasing angular momentum [14,23]. For intermediate mass nuclei around $N = 50$ an almost linear decrease of λ is found for the whole ground state band [23] whereas for lighter nuclei the decreasing trend of λ changes to an increasing λ for states above $L \approx 6$ [14].

The formalism for the calculations has been provided in earlier work [14,18,21,23]. Reduced widths γ^2_α are determined using the same method as in S&M.

3 Results and Discussion

The results for ^{46}Cr and ^{54}Cr are summarized in Tables 1 and 2. For comparison, also the results of S&M are listed in Tables 1 and 2. The potentials are shown in Fig. 1.

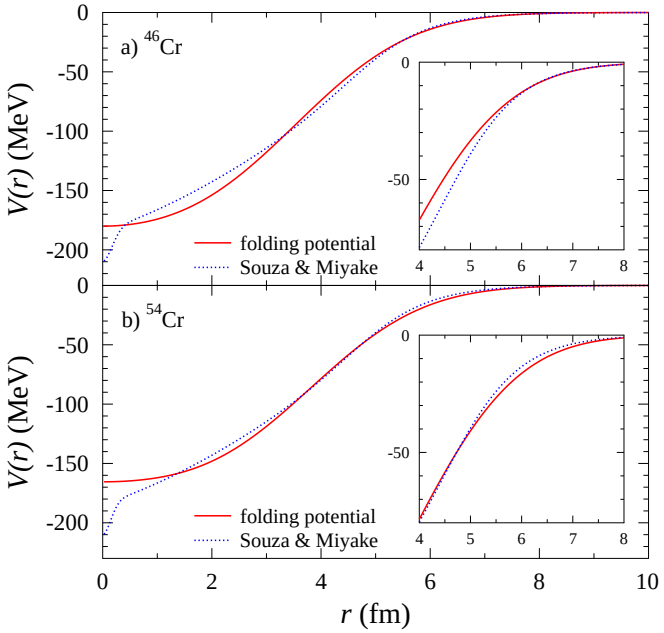

Fig. 1. Comparison between the folding potential $\lambda \times V_F(r)$ and the specially shaped potential of S&M for ^{46}Cr (upper) and ^{54}Cr (lower). The values for λ are taken from the ground states (see Tables 1 and 2). The insets enlarge the region of the nuclear surface which is most relevant for elastic scattering.

In general, good agreement is found between the present calculations in the folding model and the previous results by S&M using a specially shaped potential which was optimized for the reproduction of excitation energies. This specially shaped potential of S&M is composed of a Woods-Saxon (WS) plus a cubed WS^3 potential (as originally suggested in [39]) which is further modified by a

Table 1. α-cluster properties of ^{46}Cr. For comparison, the second line for each state shows the results of S&M [1] . Experimental data have been taken from the ENSDF database [36] which is based on [37] for ^{46}Cr.

J^π	E^* (keV)	E (keV)	N	L	λ	J_R (MeV fm^3)	$\langle R^2\rangle^{1/2}$ (fm)	γ_α^2 (keV)	θ_α^2 (%)	$B(E2, L\to L-2)$ (W.u.)	$B(E2)_{\rm exp}$ (W.u.)
0^+	0.0	−6793.8	6	0	1.2330	355.10	4.416	2.607	0.843	–	
							4.339	2.179	0.692	–	
2^+	892.2	−5901.6	5	2	1.2241	352.54	4.416	2.589	0.822	10.3	19(4)
							4.341	2.213	0.702	9.7	
4^+	1987.1	−4806.7	4	4	1.2204	351.48	4.367	1.937	0.615	13.9	
							4.299	1.690	0.536	13.0	
6^+	3226.9	−3566.9	3	6	1.2232	352.28	4.270	1.037	0.329	13.2	
							4.219	0.935	0.297	12.5	
8^+	4817.4	−1976.4	2	8	1.2293	354.04	4.137	0.392	0.127	10.7	
							4.121	0.374	0.119	10.3	
10^+	6179.5	−614.3	1	10	1.2479	359.40	3.959	0.079	0.025	7.2	
							4.010	0.084	0.027	7.1	
12^+	8162.5	+1368.7	0	12	1.2657	364.52	3.766	0.008	0.003	3.6	
							3.933	0.010	0.003	3.7	

Table 2. α-cluster properties of ^{54}Cr. For comparison, the second line for each state shows the results of S&M [1] . Experimental data have been taken from the ENSDF database [36] which is based on [38] for ^{54}Cr.

J^π	E^* (keV)	E (keV)	N	L	λ	J_R (MeV fm^3)	$\langle R^2\rangle^{1/2}$ (fm)	γ_α^2 (keV)	θ_α^2 (%)	$B(E2, L\to L-2)$ (W.u.)	$B(E2)_{\rm exp}$ (W.u.)
0^+	0.0	−7927.9	6	0	1.1213	315.54	4.438	1.133	0.392	–	
							4.290	0.631	0.218	–	
2^+	834.9	−7093.0	5	2	1.1121	312.95	4.438	1.117	0.386	8.5	14.4(6)
							4.290	0.637	0.221	7.5	
4^+	1823.9	−6104.0	4	4	1.1058	311.18	4.395	0.821	0.284	11.5	26(9)
							4.249	0.471	0.163	10.0	
6^+	3222.5	−4705.4	3	6	1.0990	309.27	4.320	0.465	0.161	11.0	18(5)
							4.181	0.268	0.093	9.7	
8^+	4681.5	−3246.4	2	8	1.0976	308.87	4.202	0.173	0.060	9.0	12.8(17)
							4.089	0.101	0.035	8.0	
10^+	6726.2	−1201.7	1	10	1.0946	308.03	4.062	0.043	0.015	6.3	
							4.003	0.027	0.009	5.7	
12^+	8825.4	+897.5	0	12	1.0980	308.98	3.888	0.005	0.002	3.2	
							3.933	0.003	0.001	3.0	

(1+Gaussian) term at small radii. Interestingly, it turns out that this specially shaped potential becomes very similar to the folding potential of the present study except at very small radii (see Fig. 1). Thus, the good agreement between the calculations is not surprising. For completeness it may be noted that specially shaped Gaussian-modified Woods-Saxon potentials have also been applied successfully to elastic scattering e.g. in [40,41].

The main difference between the folding potential of the present study and the potential by S&M is the additional Gaussian dip at very small radii in the S&M potential. This dip mainly reduces the energy of the 0^+ ground state whereas states with $L > 0$ are practically not affected because of the centrifugal barrier which scales with $L(L+1)/r^2$ and thus dominates at small radii r (see also Fig. 3 of S&M).

S&M attempt to reproduce the excitation energies of all states within the yrast band by the choice of a specially shaped potential. Contrary to that approach, the folding potential in the present study requires slight adjustments of the strength parameter λ to reproduce the energies of the (quasi-)bound states under study. Strength parameters λ of about 1.22 to 1.27 are found for ^{46}Cr, and $\lambda \approx 1.10 - 1.12$ is obtained for ^{54}Cr. The variations of λ remain very small (below 4% for ^{46}Cr and below 2% for ^{54}Cr). A smooth dependence of the strength parameter λ on the angular momentum L of the bound state is found (see Fig. 2). However, there is a significant difference between ^{46}Cr and ^{54}Cr. For ^{54}Cr there is a smooth decrease of λ, and all λ values for $L \geq 6$ are practically constant within less than 1%. For ^{46}Cr a clear increase of λ is found for $L > 6$. A similarly increasing λ for large L was also found for α-cluster states in ^{44}Ti [18].

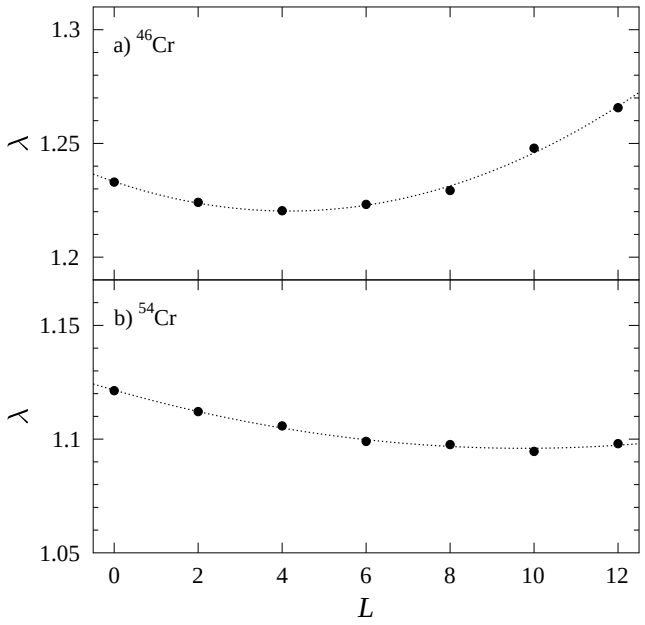

Fig. 2. Variation of the potential strength parameter λ as a function of L. Minor variations for λ are found for ^{46}Cr (below 4%, upper part) and and for ^{54}Cr (below 2%, lower part). The lines are quadratic fits.

The L dependence of λ can be fitted by a parabola

$$\lambda(L) = \lambda_0 + \Delta\lambda \times (L - L_0)^2 \qquad (4)$$

with the values $\lambda_0 = 1.22027$ (1.09596), $\Delta\lambda = 7.4881 \times 10^{-4}$ (2.6875×10^{-4}), and $L_0 = 4.1566$ (9.7575) for ^{46}Cr (^{54}Cr). The deviation between the parabolic fit in Eq. (4) and the λ values in Tables 1 and 2 is typically of the order of 0.001 or below, corresponding to energy shifts of less than 100 keV. Thus, the experimental excitation energies of the yrast bands in ^{46}Cr and ^{54}Cr can be nicely reproduced in the folding potential model in combination with a three-parameter parabolic fit for the potential strength parameter λ.

The experimental and calculated level schemes of ^{46}Cr and ^{54}Cr are shown in Figs. 3 and 4. The folding potential with constant strength (λ adjusted to the 0^+ ground states) shows a compressed rotational spectrum, in particular for states with small L. A perfect reproduction of the excitation energies is obtained using the slightly L-dependent strength parameter $\lambda(L)$ in Eq. (4). The potential by S&M describes the excitation energies, too.

For completeness it has to be noted that the reproduction of excitation energies (as shown in Figs. 3 and 4) is not trivial. Usual Woods-Saxon potentials show the trend of spectral inversion, i.e. excited states with $J > 0$ are located below the 0^+ ground state (e.g., [23]). Using typical parameters like $R = 1.3$ fm and $a = 0.65$ fm for ^{46}Cr (^{54}Cr), the first 2^+ state is found at -0.16 MeV (-0.22 MeV), and the 12^+ state appears at -8.62 MeV (-9.88 MeV). The situation becomes even worse as soon as Woods-Saxon parameters are chosen which were adjusted to elastic scattering. E.g., the geometry of

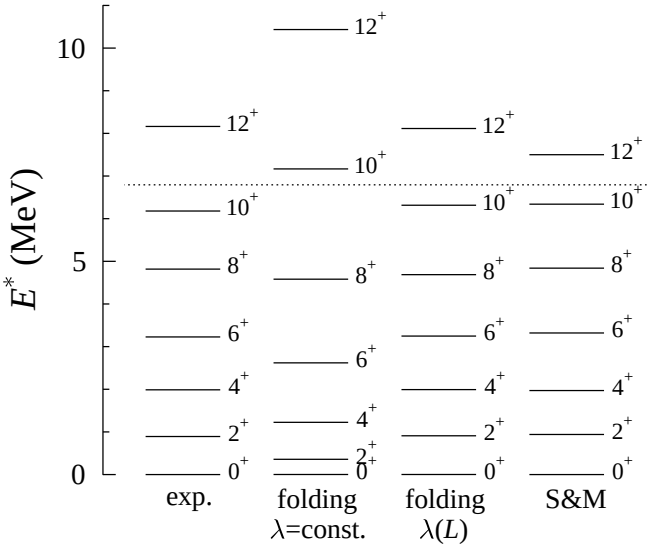

Fig. 3. Experimental and calculated level scheme of ^{46}Cr. The dashed horizontal line indicates the α threshold. The level scheme has been calculated from the folding potential with a fixed strength parameter $\lambda = 1.233$ and using $\lambda(L)$ from Eq. (4). The recent results of S&M are also shown.

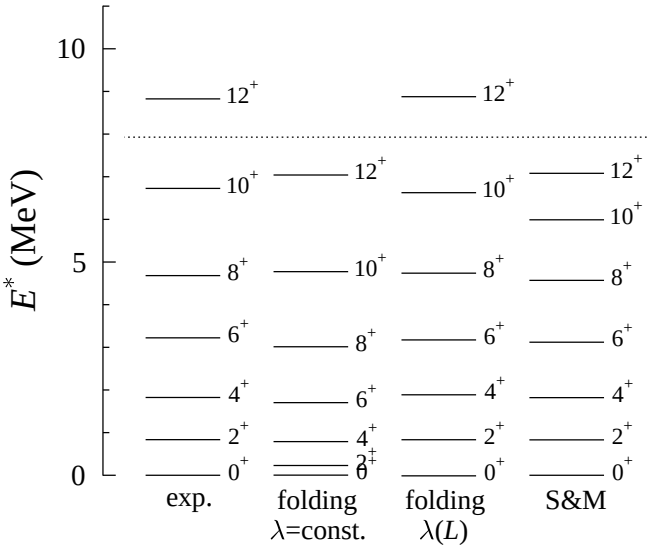

Fig. 4. Experimental and calculated level scheme of ^{54}Cr. The dashed horizontal line indicates the α threshold. The level scheme has been calculated from the folding potential with a fixed strength parameter $\lambda = 1.121$ and using $\lambda(L)$ from Eq. (4). The recent results of S&M are also shown.

the widely used potential by McFadden and Satchler [42] ($R = 1.4$ fm, $a = 0.52$ fm) leads to excitation energies of the 2^+ state of -0.36 MeV (-0.40 MeV) for ^{46}Cr (^{54}Cr). Thus, results from usual Woods-Saxon potentials are not included in Figs. 3 and 4.

As soon as the potential strength is determined by adjustment of the strength parameter λ, the corresponding wave functions $u(r)$ can be calculated by numerical solution of the Schrödinger equation. Reduced widths γ_α^2 and

θ_α^2, *rms* intercluster separations $\langle R^2\rangle^{1/2}$, and $B(E2)$ transition strengths result directly from these wave functions (similar to S&M). Qualitatively, the general findings of S&M are reproduced in the present study:
(*i*) The *rms* intercluster separation decreases slightly with increasing angular momentum L.
(*ii*) The reduced widths γ_α^2 and θ_α^2 decrease significantly with increasing L.
(*iii*) α-clustering is more pronounced in ^{46}Cr compared to ^{54}Cr.
Similar results have been obtained in earlier studies for the neighboring nucleus ^{44}Ti and also for heavier nuclei (e.g., [43,20,44,45]).

However, there are also some differences between the work of S&M and the present study. The *rms* intercluster separations are slightly larger in the present double-folding model. This holds in particular for states with small angular momentum L where smaller values in S&M result from the Gaussian dip at small radii. In the present work the reduced widths θ_α^2 are about 20% higher for states with low L in ^{46}Cr and almost a factor of two higher for ^{54}Cr. $B(E2)$ transition strengths are also slightly higher (of the order of 10%) in the present study. Furthermore, it should be pointed out that the calculated $B(E2)$ transition strengths agree reasonably well with the experimental data (whenever available). Similar to the work of S&M, no effective charges are required here.

The *rms* intercluster separations require a special discussion. Typically, strong α-cluster states are characterized by large *rms* intercluster separations $\langle R^2\rangle^{1/2}$ (as also found by S&M). The present results in Tables 1 and 2 indicate that the $\langle R^2\rangle^{1/2}$ are close and even slightly larger for ^{54}Cr with its smaller reduced widths θ_α^2. However, as soon as the radii $\langle R^2\rangle^{1/2}$ are normalized to the radius of the compound radius by $A_C^{1/3}$, these reduced radii $\langle R^2\rangle^{1/2}/A_C^{1/3}$ show the expected behavior and are larger for ^{46}Cr. So I do not provide a detailed discussion on the intercluster radii $\langle R^2\rangle^{1/2}$ because the results are not unique.

4 Analysis of elastic scattering

Finally, it is interesting to test the α-cluster potentials for ^{50}Ti(α,α)^{50}Ti elastic scattering. Here I first focus on the angular distribution at $E_\alpha = 25.0$ MeV by Gubler *et al.* [33] which is available from the EXFOR database [46]. This angular distribution covers the full angular range from about 22° to 174° in the center-of-mass system and is thus well-suited for the determination of the optical potential. In addition, it has been shown for the neighboring ^{40}Ca(α,α)^{40}Ca scattering that the optical potential at low energies ($E_\alpha = 29$ MeV) is very close to the α-cluster potential which describes the ^{44}Ti ground state band [18]. For completeness, angular distributions at 104 MeV [35] and 140 MeV [34] will also be analyzed. Unfortunately, elastic (α,α) scattering data are not available for the radioactive ^{42}Ti nucleus.

As a first step of the optical model analysis of the ^{50}Ti(α,α)^{50}Ti elastic scattering angular distribution at 25 MeV, a phase shift fit (according to the technique of [47]) was performed, and it is found that the experimental angular distribution can be very well reproduced (see Fig. 5). Next, optical model fits have been performed with the α-cluster potential as a starting point for the real part. In extension to the real potential in Eq. (2), a phenomenological potential in the imaginary part was used which is taken as the sum of volume and surface Woods-Saxon potentials:

$$W(r) = W_V \times f_{\rm WS}(x_V) + W_S \times \frac{df_{\rm WS}(x_S)}{dx_S} \qquad (5)$$

with

$$f_{WS}(x_{V,S}) = \frac{1}{1+\exp\left(x_{V,S}\right)} \qquad (6)$$

and $x_{V,S} = (r - R_{V,S} \times A_T^{1/3})/a_{V,S}$. The depths W_V, W_S, radii R_V, R_S, and diffusenesses a_V, a_S of the volume and surface part have been adjusted to the experimental angular distribution. Note that in the above definition the maximum depth of the surface part is $-W_S/4$.

A further small modification of the width of the folding potential in the real part in Eqs. (1) and (2) is introduced:

$$V_N(r) = \lambda\, V_F(r/w) \qquad (7)$$

Here w is a width parameter which should remain very close to unity (see further discussion below).

Various fits for the angular distribution at 25 MeV [33] are shown in Fig. 5. The parameters of all fits are listed in Tables 3 and 4.

The folding potential which is based on the experimental charge density distribution of ^{50}Ti does not exactly match the diffraction pattern in the forward region. The maxima and minima of the theoretical angular distribution are shifted towards larger angles; this corresponds to a potential which is slightly too narrow. After scaling the radial dependence of the real potential by a factor of $w = 1.02$ a much better fit is obtained (for technical details, see [29]). Such a behavior is not surprising for ^{50}Ti with $N/Z \approx 1.27$ because the neutron distribution should have a larger radial extent than the proton (charge) distribution. Evidence for a larger radial extent of the neutron distribution of ^{50}Ti was also derived from α scattering at higher energies [48].

Fortunately it turns out that the folding potential which is calculated from the theoretical density distribution of ^{50}Ti (as provided in TALYS) is able to reproduce the experimental angular distribution without a significant radial scaling (the best fit is obtained using a scaling parameter of $w = 0.997$, i.e., very close to unity). This confirms the reliability of the theoretical density distribution of ^{50}Ti which is consequently used throughout this paper.

The best-fit potential shows a real volume integral of $J_R \approx 342$ MeV fm^3 and $r_{R,rms} \approx 4.39$ fm; the imaginary part has $J_I \approx 67$ MeV fm^3 and $r_{I,rms} \approx 4.45$ fm. (As usual, the negative sign of the volume integrals is neglected in the discussion of J_R and J_I.) The real volume

Table 3. Parameters of the real part of the optical potential and integral values.

E_α (MeV)	type	$\rho(^{50}\mathrm{Ti})$	λ –	w –	J_R (MeV fm^3)	$r_{R,rms}$ (fm)	J_I (MeV fm^3)	$r_{I,rms}$ (fm)	σ_R (mb)
25.0	fold.	exp. [30]	1.246	$\equiv 1.000$	324.9	4.305	63.5	4.580	1395
25.0	fold.	exp. [30]	1.247	1.020	345.1	4.391	66.8	4.409	1337
25.0	fold.	theo. [32]	1.294	0.997	341.8	4.388	67.4	4.448	1343
25.0	S&M		–	–	301.1	4.323	68.5	4.646	1404
104.0	fold.	theo. [32]	1.249	0.990	289.8	4.377	88.2	5.037	1557
104.0	S&M		–	–	301.1	4.323	92.2	4.754	1413
140.0	fold.	theo. [32]	1.237	1.016	290.3	4.505	94.9	5.275	1687
140.0	S&M (V1)		–	–	301.1	4.323	239.4	4.649	1638
140.0	S&M (V2)		–	–	301.1	4.323	115.0	5.302	1805

Table 4. Parameters of the imaginary part of the optical potential.

E_α (MeV)	type	$\rho(^{50}\mathrm{Ti})$	W_V (MeV)	R_V (fm)	a_V (fm)	W_S (MeV)	R_S (fm)	a_S (fm)
25.0	fold.	exp. [30]	−19.6	1.385	0.263	+4.2	1.876	0.591
25.0	fold.	exp. [30]	−21.7	1.355	0.191	+9.2	1.741	0.391
25.0	fold.	theo. [32]	−21.7	1.353	0.185	+9.7	1.746	0.406
25.0	S&M		−20.9	1.386	0.220	+6.1	1.958	0.457
104.0	fold.	theo. [32]	−21.0	1.400	0.547	+14.8	1.631	0.608
104.0	S&M		−23.1	1.458	0.368	+12.0	1.691	0.459
140.0	fold.	theo. [32]	−21.4	1.296	0.519	+24.5	1.544	0.765
140.0	S&M (V1)		−67.2	1.413	0.204	+41.0	1.830	0.320
140.0	S&M (V2)		−26.6	2.106	0.715	−74.6[a]	1.793	0.783

[a]Note that the sum of volume and surface imaginary potential does not change its sign.

integral J_R from elastic scattering is close to the results from scattering on neighboring nuclei [18] but significantly larger than the values for the α-cluster states which are around $310 - 315$ MeV fm^3 (see Table 2). For very pronounced α-cluster nuclei like ^{44}Ti or ^{20}Ne such deviations are neither expected nor found [18,14], and thus this deviation for ^{54}Cr may be interpreted that ^{54}Cr is not a very pure $^{50}\mathrm{Ti} \otimes \alpha$ cluster. This interpretation is in agreement with the smaller reduced widths which are found for ^{54}Cr (in comparison to ^{46}Cr and ^{44}Ti).

As the potential by S&M has been optimized for the description of α-cluster states with low $J_R \approx 300$ MeV fm^3, it is not surprising that this potential cannot reproduce the $^{50}\mathrm{Ti}(\alpha,\alpha)^{50}\mathrm{Ti}$ angular distribution with similar quality as the double-folding potentials. Furthermore, $r_{R,rms} = 4.32$ fm of the S&M potential is also lower than the best-fit values around 4.39 fm by about 2%.

At higher energies the differences between the folding potential and the potential by S&M become even more obvious. Indeed, the volume integral J_R and the *rms* radius of the S&M potential are close to the results of Roberson *et al.* at $E_\alpha = 140$ MeV [34]. However, angular distributions at higher energies are not only sensitive to the potential at the nuclear surface but depend on the shape of the potential in a wider radial range. In the following I analyze the angular distributions at 140 MeV by Roberson *et al.* [34] and at 104 MeV by Pesl *et al.* [35]. Unfortunately, the 140 MeV data (as provided by EXFOR) had to be re-read from Fig. 1 of [34]; this leads to increased uncertainties and lower reliability of the extracted parameters. As no uncertainties are provided in EXFOR, a fixed uncertainty of 5% was assumed for the fitting procedure. Furthermore, the angular range of the 140 MeV data is limited to about 75°, and the number of data points (51) is not very high. The angular distribution at 104 MeV [35] covers a larger angular range up to 90°, consists of a factor of three more data points, and is available numerically (including uncertainties) from the internal report KFK-3242 [49].

The 140 MeV data can be nicely reproduced by the folding potential (see Fig. 6). The resulting volume integrals J_R and J_I are close to the results obtained for neighboring nuclei [18]: J_R decreases with increasing energy, and J_I approaches a saturation value of about 100 MeV fm^3. An early study with folding potentials has also determined similar volume integrals [50]. Thus, the present analysis mainly confirms that the chosen theoretical density of ^{50}Ti in combination with the DDM3Y interaction is appropriate.

Keeping a fixed real part from S&M and adjusting only the imaginary potential leads to a significantly worse reproduction of the experimental angular distribution. The best fit shows a strongly oscillating angular distribution at backward angles, correlated with very different imaginary volume integral J_I. It is obvious from Fig. 6 that the strongly oscillating backward cross sections are not sufficiently constrained by the few experimental data points above about 50°. A further local minimum in χ^2 can be found with reasonable volume integrals (V2 in Fig. 6 and Tables 3 and 4); however, this results in a relatively poor reproduction of the experimental data at forward angles.

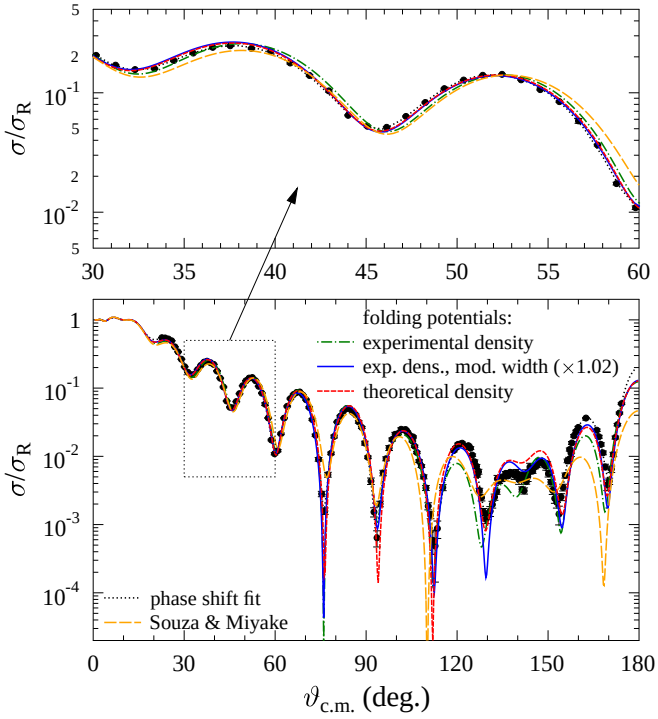

Fig. 5. Analysis of the angular distribution of ^{50}Ti(α,α)^{50}Ti elastic scattering at 25 MeV (normalized to Rutherford scattering) [33,46]: The phase shift fit (black dotted) reproduces the experimental data almost perfectly (thus, it is practically invisible behind the experimental data). The folding potential using the experimental charge density distribution of ^{50}Ti (green dash-dotted) is slightly too narrow, resulting in a poor description of the forward angle diffraction pattern (see enlarged area in the upper plot); a better description of the experimental data is obtained after scaling the radial dependence by 2% (full blue). The folding potential using the theoretical ^{50}Ti density (short-dashed red) is able to describe the experimental data without significant radial modification. The potential of S&M is again too narrow and has a lower J_R, leading to deviations in the forward angle diffraction pattern and at backward angles (long-dashed orange).

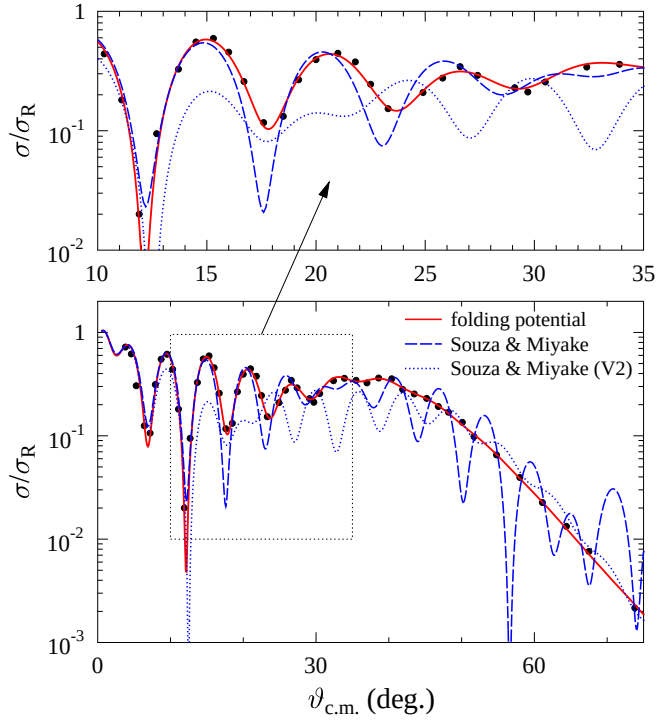

Fig. 6. Analysis of the angular distribution of ^{50}Ti(α,α)^{50}Ti elastic scattering at 140 MeV (normalized to Rutherford scattering) [34,46]. The experimental data are nicely reproduced using a folding potential (full red line) whereas two different fits (dashed and dotted blue lines) with the fixed S&M potential in the real part show larger deviations. Further discussion see text.

Also the angular distribution at 104 MeV [35] is very well reproduced by the folding potential (see Fig. 7). Interestingly, the width parameter for the 104 MeV data is very close (within 0.7%) to the 25 MeV fit. For the 140 MeV data the resulting width parameter was about 2% higher. This finding may have been affected from the uncertainties of the re-digitization of the 140 MeV data and the missing experimental uncertainties.

The fit with the fixed S&M real part results in volume integrals which are very close to the folding potential results. It is not surprising that the fixed S&M real part cannot reproduce the experimental angular distribution with the accuracy as the folding potential with two adjustbale parameters (strength λ and width w). But even if the same scaling parameters (λ and w) are applied to the S&M potential, it is not possible to reproduce the angular distribution with a similar quality as the folding potential.

Summarizing the above analysis of elastic scattering angular distributions, it can be stated that the folding potential is able to describe the angular distributions over a wide energy range with smoothly varying parameters. The width parameter w remains very close to unity using a theoretical density of ^{50}Ti whereas a folding potential derived from the experimental charge distribution requires a radial scaling of about 2%.

The potential of S&M is close to the folding potential whose parameters have been adjusted to elastic scattering angular distributions. This is a quite noticeable finding because the S&M potential was optimized only for the reproduction of excitation energies of ^{54}Cr. Without any further adjustment of the real part, the S&M potential cannot reach the same accuracy in the reproduction of the angular distributions, but it still provides a reasonable description of the experimental data at 25 MeV and 104 MeV.

5 Summary and conclusions

α-cluster states in ^{46}Cr and ^{54}Cr are studied on the basis of a double-folding potential. A minor and smooth variation of the potential strength is found for the states under study in ^{46}Cr and ^{54}Cr. Reduced widths, intercluster

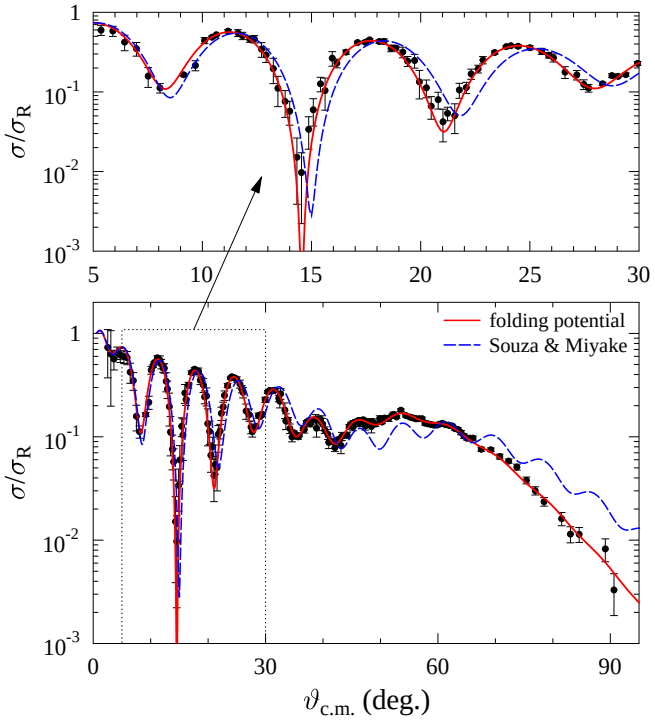

Fig. 7. Analysis of the angular distribution of ^{50}Ti(α,α)^{50}Ti elastic scattering at 104 MeV (normalized to Rutherford scattering) [35,46]. Similar to the 140 MeV data, the folding potential (full red line) reproduces the experimental angular distribution, but the S&M potential (dashed blue line) shows larger deviations. Further discussion see text.

separations, and transition strengths are close to the results of a recent study by Souza and Miyake [1] using a specially shaped potential, and the calculated transition strengths show reasonable agreement with the experimental values without effective charges. The present study confirms the significant α-cluster properties of ^{46}Cr and smaller reduced widths for ^{54}Cr. Furthermore, it is found that the specially shaped potential by S&M is close to the double-folding potential of the present study (except at very small radii).

The application of the double-folding potential to elastic ^{50}Ti(α,α)^{50}Ti scattering provides excellent fits for the angular distributions over a wide energy range from 25 MeV to 140 MeV. The derived parameters show that the underlying ^{50}Ti density should be preferentially taken from theory. The potential which is calculated from the experimental charge density distribution, turns out to be too narrow by about 2%, thus indicating a larger radial extent of the neutron distribution in ^{50}Ti.

Acknowledgments

I thank M. A. Souza and H. Miyake for providing their results amd for encouraging discussions. This work was supported by OTKA (K108459 and K120666).

References

1. M. A. Souza and H. Miyake, Europ. Phys. J. A **53**:146 (2017)
2. H. Horiuchi, K. Ikeda, K. Katō, Prog. Theor. Phys. Suppl. **192**, 1 (2012).
3. S. Ohkubo, M. Fujiwara, P. E. Hodgson, Prog. Theor. Phys. Suppl. **132**, 1 (1998).
4. F. Michel, S. Ohkubo, G. Reidemeister, Prog. Theor. Phys. Suppl. **132**, 7 (1998).
5. T. Yamaya, K. Katori, M. Fujiwara, S. Kato, S. Ohkubo, Prog. Theor. Phys. Suppl. **132**, 73 (1998).
6. T. Sakuda and S. Ohkubo, Prog. Theor. Phys. Suppl. **132**, 103 (1998).
7. E. Uegaki, Prog. Theor. Phys. Suppl. **132**, 135 (1998).
8. M. Hasegawa, Prog. Theor. Phys. Suppl. **132**, 177 (1998).
9. S. Koh, Prog. Theor. Phys. Suppl. **132**, 197 (1998).
10. A. Tohsaki, Prog. Theor. Phys. Suppl. **132**, 213 (1998).
11. P. Descouvemont, Nucl. Phys. **A709**, 275 (2002).
12. T. Sakuda and S. Ohkubo, Nucl. Phys. **A712**, 59 (2002).
13. P. Mohr, H. Abele, V. Kölle, G. Staudt, H. Obrhummer, H. Krauss, Z. Phys. A **349**, 339 (1993).
14. H. Abele and G. Staudt, Phys. Rev. C **47**, 742 (1993).
15. S. Wilmes, V. Wilmes, G. Staudt, P. Mohr, J. W. Hammer, Phys. Rev. C **66**, 065802 (2002).
16. P. Mohr, Phys. Rev. C **72**, 035803 (2005).
17. P. Mohr, C. Angulo, P. Descouvemont, H. Utsunomiya, Europ. Phys. J. A 27, s01, 75 (2006).
18. U. Atzrott, P. Mohr, H. Abele, C. Hillenmayer, and G. Staudt, Phys. Rev. C **53**, 1336 (1996).
19. F. Hoyler, P. Mohr, G. Staudt, Phys. Rev. C **50**, 2631 (1994).
20. S. Ohkubo, Phys. Rev. Lett. **74**, 2176 (1995).
21. P. Mohr, Europ. Phys. J. A **31**, 23 (2007).
22. S. Ohkubo, Int. J. Mod. Phys. A **14**, 2035 (2009).
23. P. Mohr, The Open Nuclear and Particle Physics Journal **1**, 1 (2008).
24. P. Mohr, Phys. Rev. C **61**, 045802 (2000).
25. Chang Xu and Zhongzhou Ren, Phys. Rev. C **73**, 041301(R) (2006).
26. P. Mohr, Phys. Rev. C **95**, 011302(R) (2017).
27. G. R. Satchler and W. G. Love, Phys. Rep. **55**, 183 (1979).
28. A. M. Kobos, B. A. Brown, R. Lindsay, and G. R. Satchler, Nucl. Phys. **A425**, 205 (1984).
29. P. Mohr, G. G. Kiss, Zs. Fülöp, D. Galaviz, Gy. Gyürky, E. Somorjai, At. Data Nucl. Data Tables **99**, 651 (2013).
30. H. de Vries, C. W. de Jager, and C. de Vries, Atomic Data and Nuclear Data Tables **36**, 495 (1987).
31. K. Tsukuda *et al.*, Phys. Rev. Lett. **118**, 262501 (2017).
32. A. J. Koning, S. Hilaire, S. Goriely, computer code TALYS, version 1.8, *http://www.talys.eu*; A. J. Koning, S. Hilaire, and M. C. Duijvestijn, AIP Conf. Proc. **769**, 1154 (2005).
33. H. P. Gubler, U. Kiebele, H. O. Meyer, G. R. Plattner, I. Sick, Nucl. Phys. **A351**, 29 (1981).
34. P. L. Roberson, D. A. Goldberg, N. S. Wall, L. W. Woo, H. L. Chen, Phys. Rev. Lett. **42**, 54 (1978).
35. R. Pesl, H. J. Gils, H. Rebel, E. Friedman, J. Buschmann, H. Klewe-Nebenius, S. Zagromski, Z. Phys. A **313**, 111 (1983).
36. Online database ENSDF, available at *www.nndc.bnl.gov/ensdf*; based on [37,38].
37. S.-C. Wu, Nucl. Data Sheets **91**, 1 (2000).

38. Yang Dong and Huo Junde, Nucl. Data Sheets **121**, 1 (2014).
39. B. Buck, A. C. Merchant, S. M. Perez, Phys. Rev. C **51**, 559 (1995).
40. F. Michel, J Albinski, P. Belery, Th. Delbar, Gh. Grégoire, B. Tasiaux, G. Reidemeister, Phys. Rev. C **28**, 1904 (1983).
41. F. Michel, G. Reidemeister, S. Ohkubo, Phys. Rev. C 61, 041601(R) (2000).
42. L. McFadden and G. R. Satchler, Nucl. Phys. **84**, 177 (1966).
43. M. A. Souza and H. Miyake, Phys. Rev. C **91**, 034320 (2015).
44. F. Michel, G. Reidemeister, S. Ohkubo, Phys. Rev. C **37**, 292 (1988).
45. B. Buck, C. B. Dover, J. P. Vary, Phys. Rev. C **11**, 1803 (1975).
46. N. Otuka *et al.*, Nucl. Data Sheets **120**, 272 (2014); EXFOR database available online at *http://www-nds.iaea.org/exfor/exfor.htm*.
47. V. Chisté, R. Lichtenthäler, A. C. C. Villari, L. C. Gomes, Phys. Rev. C **54**, 784 (1996).
48. H. J. Gils, H. Rebel, E. Friedman, Phys. Rev. C **29**, 1295 (1984).
49. R. Pesl, internal report KFK-3242, Kernforschungszentrum Karlsruhe (1982); available at *https://publikationen.bibliothek.kit.edu/270016791*.
50. A. M. Kobos, B. A. Brown, P. E. Hodgson, G. R. Satchler, A. Budzanowski, Nucl. Phys. **A384**, 65 (1982).